Heliyon 9 (2023) e19930

Contents lists available at ScienceDirect

Heliyon

journal homepage: www.cell.com/heliyon

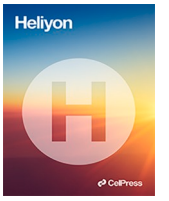

Structural modification of WC-Co cutting tools by laser doping treatment

Yayoi Tanaka *, Hisashi Sato, Osamu Eryu

Nagoya Institute of Technology, Gokiso-cho, Showa-ku, Nagoya, Aichi, 466-8555, Japan

ARTICLE INFO

Keywords:
Laser doping
Carbides
Cemented carbide
Surfaces
Electron backscatter diffraction

ABSTRACT

We have previously shown that sharpening the cutting edge of a cemented carbide tool by chemical-mechanical polishing (CMP) improved the cutting speed by approximately 150% and reduced the wear on the flank surface by approximately 50% compared to a commercial tool when cutting a heat-resistant alloy. In addition, the cutting edges of carbide tools treated by laser doping (LD) using boron nitride as doping material achieved approximately 100 times longer cutting distance in glass machining than the edges of carbide tools treated with CMP grinding wheels. In this study, LD was conducted on a tool base material (WC–Co) to investigate and understand the crystal structure changes of the base material upon treatment. Electron backscatter diffraction and X-ray diffraction results show that the effect of LD was observed in the region 50 nm below the surface. LD improved the strength by approximately 11.7% without destroying the surface crystal structure. Thus, doping can be performed on tool tips while maintaining the WC structure to improve the performance of WC-Co cutting tools.

1. Introduction

Cemented carbide WC-Co is commonly used as a cutting tool [1] for machining ferrous materials [2,3] owing to its excellent hardness and toughness. When cutting with machine tools, the dimensional accuracy of the workpiece depends on parameters such as cutting speed. Moreover, the dimensional accuracy and surface roughness of the workpiece after machining are strongly influenced by the deterioration of the cutting tool.

When WC-Co is shaped into a cutting tool, the diamond grinding wheel used for shaping cutting edges causes latent damage owing to diamond abrasive grains, which are observed at a depth of several tens of micrometers [4,5], and reduces the strength of the material [6,7]. A latent scratch on the cutting edge induces chipping of the edge during cutting [2]. Moreover, as the wear of the cutting edge progresses because of the increase in the contact area between the cutting edge and workpiece, the surface temperature of the workpiece and cutting tool increases owing to frictional heat, subsequently melting the material and leading to processing strain and adhesion [3,8–12]. Therefore, we focused on the removal of latent defects through semiconductor polishing [13,14] and developed a chemical-mechanical polishing (CMP) grinding wheel that can polish latent defect layers [6,7].

The developed CMP wheel sharpens the cutting tool without latent scratches [6,7]. However, sharpening the cutting edge does not completely suppress chemical reactions during the cutting process. Cemented carbide tools such as WC-Co have high hardness; however, Co is highly reactive and tends to be the starting point of adhesion. Hence, such tools are not suitable for cutting extremely

* Corresponding author.
E-mail address: y.tanaka.547@stn.nitech.ac.jp (Y. Tanaka).

https://doi.org/10.1016/j.heliyon.2023.e19930
Received 5 June 2023; Received in revised form 5 September 2023; Accepted 6 September 2023
Available online 10 September 2023

hard materials [15]. Although coatings [10,16–18] are applied to suppress the chemical reactivity of the tool edge to the workpiece, the latent scratch layer on the WC-Co surface peels off with the coating during cutting.

To improve the interfacial bond strength between the cutting tool edge and coating, researchers have developed surface modification techniques such as microblasting [19,20], laser peening [21], microstructural and surface modification using pulsed lasers [22–24], and Co removal [25]. In addition to improving the bond strength between the cutting tools and coatings, blast polishing [26], surface modification and microstructure formation using femtosecond lasers [27,28], laser peening [29], and surface modification with high-intensity pulse ion beams [30] have been attempted. However, in laser treatment, the cutting tool surface undergoes annealing, which reduces the surface strength [31]. Furthermore, the microstructure formed on the cutting tools causes chipping during cutting [32]. Meanwhile, ion beam treatment at high energy densities has been reported to reduce the WC-Co surface hardness [30]. Ion beam treatment at high energy densities causes crystal displacement because of atomic scattering caused by atomic collisions. Thus, the destruction of the WC structure reduces the hardness of the WC-Co surface.

In a previous study, a CMP grinding wheel [6,7] was used to sharpen carbide tools and remove the latent scratch layer on the cutting edge. A newly developed laser doping (LD) process was then conducted to extend the service life of the tools. Boron nitride (BN) was selected as the doping material because it can suppress chemical reactions with the workpiece to improve tool life. Bushlya et al. reported that simply changing from a carbide tool to a PCBN tool can facilitate machining Inconel718 at three to five times the cutting speed [16]. Modifying the cemented carbide surface layer by doping with elements other than WC-Co [33] is expected to inhibit chemical reactions with the workpiece and extend the life of cutting tools. For instance, glass was cut using LD-treated cemented carbide tools to suppress chemical reactions and extend the service life [34]. LD treatment can extend the life of WC-Co without destroying its structure. However, the mechanism by which LD treatment affects the crystal structure of the cutting tool base material must still be clarified for the industrial application of this technology.

This study aims to clarify how the surface structure of WC-Co is changed by LD treatment. The edge of the WC-Co tool is sharpened with a CMP grinding wheel, the latent damage layer on the edge is removed, and the tool life is extended with LD treatment.

2. Materials and methods

The structural change by LD was investigated using cemented carbide tool (DNGA150404 HTi10, WC-Co, WC: 94%, Co: 6%) manufactured by Mitsubishi Materials Corporation. To analyze the surface crystal structures through electron backscatter diffraction (EBSD), the sample was cut with a diamond blade (0.3 mm thick, #170 gr size: 88 μm) at a thickness of 1 mm [7]. The cutting resistance of diamond blades could be divided into two main types among the 10-piece carbide tools: easy or difficult cutting, depending on the Vickers hardness as discussed in Section 3.1.3. Before LD, the surface was flattened using the developed CMP grinding wheel [6,7]. Resinoid (phenolic) grinding wheels were prepared by mixing oxidants with green silicon carbide (GC, powder, Fujimi Incorporated) [7]. The WC-Co surface was finished with #240 to #30,000 CMP grinding wheels. The whetstone count was determined using the GC average particle size. The WC surface structure is free of electronic defects, maximizing the material properties and producing the toughness and hardness required for cutting tools [14]. Prior to all analyses, the samples were sonicated in ultrapure water (18.2 MΩ cm) for 10 min and kept in vacuum (below −0.1 MPa) for 24 h. SEM (JSM -7800 F, JEOL Ltd.) measurements were made using a field emission scanning electron microscope (FE-SEM). SEM images were observed from secondary electrons at an acceleration voltage of 5 kV. Energy-dispersive X-ray spectrometry (EDS, EDS detector: X-Max 80, Oxford Instruments) was performed at an acceleration voltage of 5 kV to monitor the elemental (W Mα1, C Kα1, Co Lα1,2, BKα1_2, N Kα1_2, OKα1)

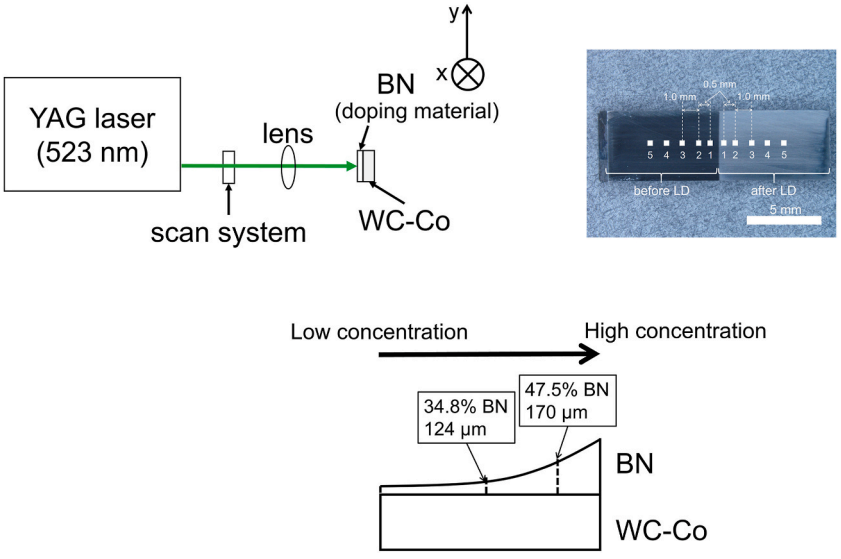

Fig. 1. Schematic of the optical system. The photograph illustrates the sample with the points where Vickers hardness values were measured.

distribution on the surface before and after LD. The EDS measurements were analyzed using Aztec 4.4 (Oxford Instruments). Moreover, the EBSD (EBSD camera: Digi View TSL solutions Corporation) measurement conditions were as follows: acceleration voltage of 15 kV; step size of 50 nm; and measurement area of 5.07 μm × 14.73 μm. The EBSD measurements were analyzed using OIM-Analysis Version 8.6 (TSL Solutions Corporation). No cleaning was used for the analysis of all EBSD data. Moreover, the X-ray diffraction (XRD, XRD-6100, Shimadzu Corporation) measurements were performed using CuKα ($\lambda = 1.5406$ Å) radiation at 40 kV and 30 mA. The scan size was 0.02° and the 2θ scan range was from 25° to 105°. Vickers hardness was measured using an automatic Vickers hardness tester (HMV-1ADW, Shimadzu Corporation) at 9.807 N (HV1) for 15 s.

A schematic of the optical system used for the LD is shown in Fig. 1. LD was performed under the same conditions as those for LD on the carbide tools in a previous study [34]. A YAG laser (532 nm) with an irradiation energy of 50 μJ, a pulse width of 550 ps, and a repetition frequency of 50 kHz was used for the LD treatment. The sample was irradiated at room temperature (approximately 25 °C) and in an ambient atmosphere. The scanning system for uniform laser irradiation of the substrate surface uses a galvanometer mirror (GVS 302, Thorlabs, Inc.) that vibrates at a high frequency [35]. The scan frequency (x: 139 Hz, y: 9 Hz) was determined by considering the frequency of the pulsed laser oscillation. The number of laser shots is determined by the repetition frequency and laser irradiation time. The distance between the lens and the sample was 340 mm (focal length = 400 mm).

BN powder (particle size approximately 10 μm, 99%), manufactured by Kojundo Chemical Co., Ltd., was used as the doping material. The BN powder was ground to an average particle size of 1 μm using a Desktop Pot Mill Stand (PM-001, As One Corporation). The BN powder and WC balls were placed in a stainless-steel pot mill and run for 20 h. The particle size distribution of BN powder showed a Gaussian distribution [36,37]. BN solution was prepared using milled BN powder. Isopropyl alcohol (IPA) and ethanol/ultrapure water mixtures have previously been used as solvents to disperse BN powders [38]. Ethanol was selected as the solvent for the concentration changes to ensure safety and potential industrialization. The WC-Co substrate was put into a BN solution, then removed from the BN solution and allowed to dry. As a result, BN was applied on the WC-Co substrate. Following LD, the substrate was

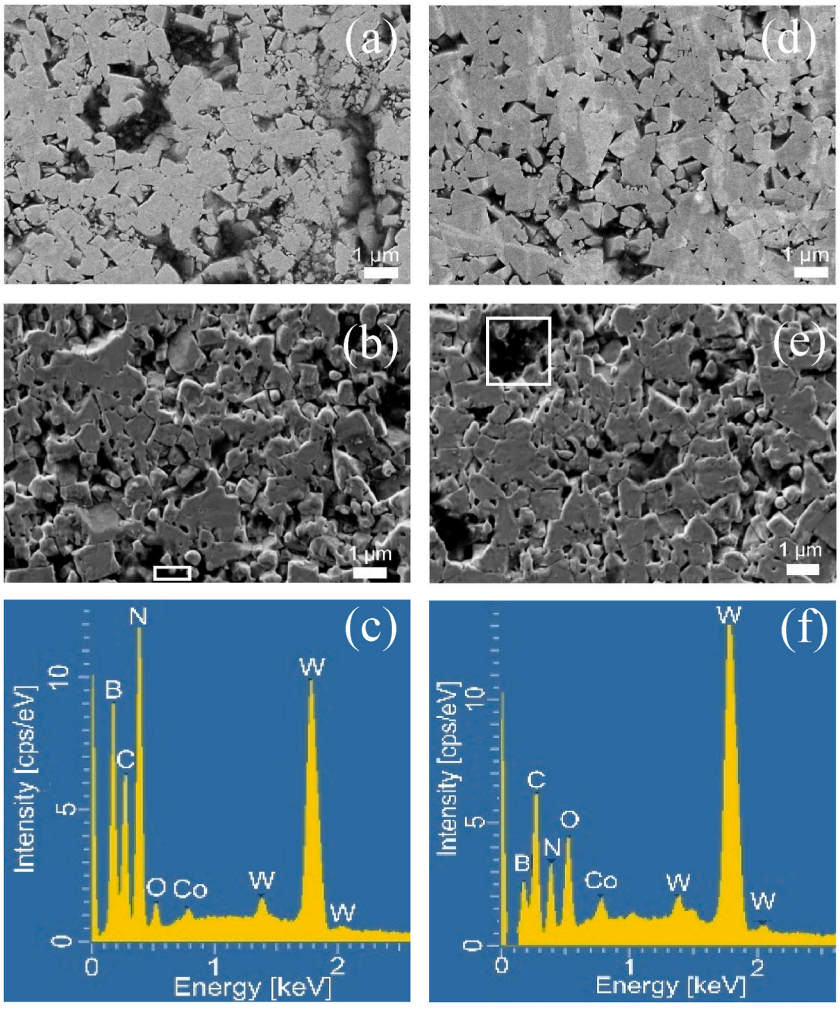

Fig. 2. SEM images of WC-Co (a, b) before and (d, e) after the LD treatment. SEM images of the (a, b, c) easy-to-cut samples and (d, e, f) difficult-to-cut samples. EDS profiles in (c) and (f) are taken from the region marked with white boxes in (b) and (e).

rinsed with ultrapure water (18.2 MΩ cm) for 10 min with ultrasonic cleaning to remove any residual BN.

LD-treated carbide tools exhibited an increased tool life by 100 times in glass processing [34]. To investigate the surface crystal structure of the carbide tool, LD was performed under the same conditions as those for previous LD-treated carbide tools [34]. The BN concentration for the LD treatment was 34.8% (8.8 ml of ethanol for 3.7 g). It should be noted that the thickness of the BN film is related to the BN concentration. At low BN concentrations (less than 34.8%), laser irradiation leads to the loss BN in the film due to the thinness of the film and the ablation action. At high BN concentrations (47.5%), the BN film is so thick that the laser light necessary for doping does not reach the interface of the BN film and WC-Co.

LD was performed at a BN concentration of 34.8% at 500,000 shots [34]. Laser irradiation (without BN) was performed for 500,000 and 1,000,000 shots to further examine the effect of LD. To investigate the difference in BN coverage, 500,000 and 10, 000, 000 shots were performed at a BN concentration of 47.5%.

3. Results and discussion

3.1. Surface structural change of WC-Co by LD-treated with 34.8% BN

3.1.1. SEM and EDS of WC-Co surface before and after LD

Fig. 2 shows the SEM images of the easy-to-cut and difficult-to-cut WC-Co surfaces before and after LD. From Fig. 2 (a) and (d), a flat WC surface can be observed on the WC-Co surface before the LD treatment. Moreover, Fig. 2 (b) and (e) show that the LD-treated WC-Co surface has convex edges. Therefore, the LD-treated WC-Co surface showed negligible change in relation to the untreated WC-Co surface. Moreover, the depth observed through EDS was estimated using an electron flight simulator Version 3.1-LV SPI (Supplies and Structure Probe, Inc.) at a density of 14.9 g/cm^3 [39,40] for WC-Co; the results are listed in Table 1.

EDS was performed on the entire SEM image shown in Fig. 2 (b) and (e). B and N were partially observed within the measurement range. The spectra of the areas where B and N were observed in the mapping (white-framed area in the SEM image) are shown in Fig. 2 (c) and (f). Moreover, Table 2 lists the atomic concentrations approximated from the spectra. The absence of B and N in the EDS profile of the untreated WC-Co surface further confirms the doping effect of LD. The photon energy of the laser beam is 2.33 eV, and the optical bandgap of BN is reported to be 5.955 eV [41]. Because the photon energy is lower than the binding energy of BN, the BN bond is not decomposed by laser irradiation. Therefore, B and N are incorporated into the WC-Co as BN. Furthermore, O was detected on the WC-Co surface after LD, which could be caused by the oxidation of the laser-irradiated WC-Co surface in the atmosphere. Both SEM and EDS results show no differences between the easy-to-cut and difficult-to-cut WC-Co surfaces.

3.1.2. EBSD and XRD of WC-Co before and after LD-treated

The surface structures of LD-treated WC-Co were studied through EBSD and XRD. EBSD was performed to observe the crystal direction from the surface to a depth of approximately 50 nm. Fig. 3 shows the EBSD results for the WC-Co surface before and after LD. Before LD, the WC-Co surface had a high CI value (Fig. 3(a-2) and (b-2)), and the WC structure was observed in the IPF map (Fig. 3(a-1) and (b-1)). Some areas of the WC-Co surface had low CI values after the LD treatment (Fig. 3(a-4) and (b-4)) and the WC structure was absent in the IPF map (Fig. 3(a-3) and (b-3)). These results indicate that LD changed the surface structure.

Fig. 4 shows the XRD patterns of the WC-Co surface before and after LD. Each XRD peak was identified using the PDF-4 database provided by the International Center for Diffraction Data. X-ray penetration lengths [42] of the WC-Co surface were estimated based on the sample density of 14.9 g/cm^3 [39,40], mass absorption coefficients (cm^2/g) for CuKα radiation for W (1.68), C (4.51), and Co (3.21) [43], and their corresponding atomic weights. The crystal structure up to a depth of approximately 0.17 mm was studied through XRD. Only the peaks derived from the WC structure were observed in the XRD patterns of the WC-Co surface before and after LD [44]. The difficult-to-cut surface showed a peak with a narrower width at half maximum than the easy-to-cut surface. However, this effect was not observed for all face orientations on the WC-Co surface before LD. Otherwise, the widths at half maximum of the difficult-to-cut and easy-to-cut samples were the same. The difficult-to-cut WC-Co surface after LD has a higher strength and narrower width at half maximum than that before LD. The narrower width at half maximum of the LD-treated WC-Co surface was caused by the annealing effect induced by laser irradiation.

The EBSD and XRD results reveal that the crystal structure of the LD-treated WC-Co surface after LD was different from that before LD. In addition, no difference was observed in the easy-to-cut and difficult-to-cut WC-Co surfaces before and after LD. The structure of the WC-Co surface after LD was found to change at a depth of ~50 nm from the surface. EDS results indicated that B and N were observed from the surface to a depth of approximately 50 nm. We believe that this change in the surface structure is due to the doping involved in LD.

3.1.3. Vickers hardness tests before and after LD-treated

Table 3 shows the Vickers hardness values of the untreated and LD-treated WC-Co surfaces at the positions shown in Fig. 1. The

Table 1
Element depth quantification results of EDS.

	W Mα1	C Kα1	Co Lα1,2	B Kα1_2	N Kα1_2	O Kα1
Depth [μm]	0.075	0.06	0.085	0.05	0.075	0.09

Table 2
Chemical composition of the samples estimated from the spectra in Fig. 2 (c) and (f).

Sample	W [at%]	C [at%]	B [at%]	O [at%]	N [at%]	Co [at%]
Easy-to-cut	42.1	35.9	6.2	6.5	5.9	3.4
Difficult-to-cut	43.9	32.4	8.0	6.7	6.3	2.7

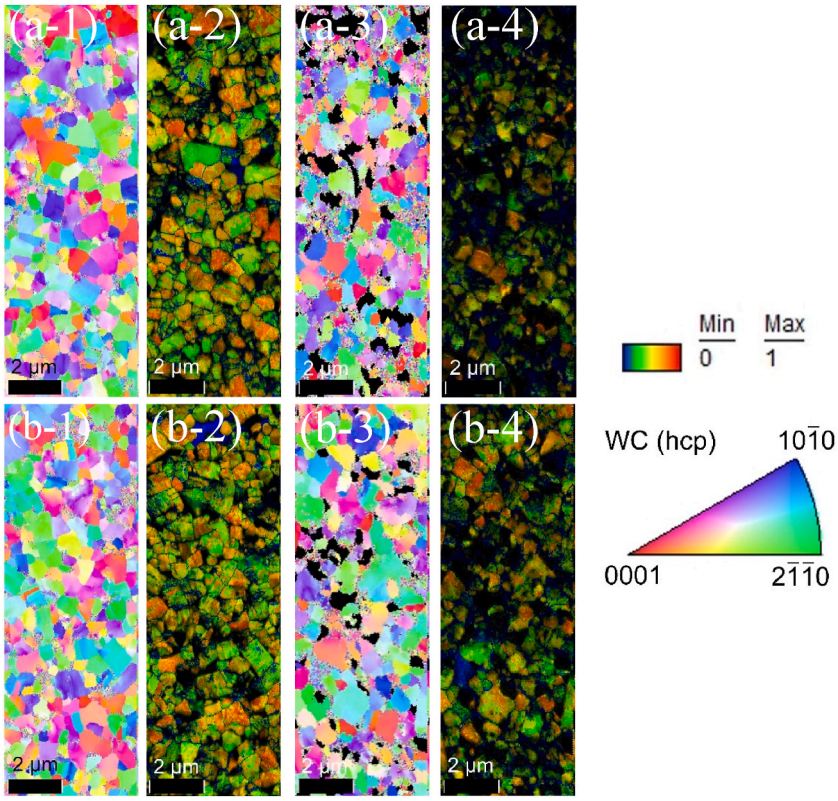

Fig. 3. EBSD results (a-1, a-2, b-1, b-2) before and (a-3, a-4, b-3, b-4) after the LD treatment. EBSD patterns of the (a-1)–(a-4) easy-to-cut and (b-1)–(b-4) difficult-to-cut samples. The IPF maps are shown in (a-1), (a-3), (b-1), and (b-3), and the CI maps are in (a-2), (a-4), (b-2), and (b-4). The colors correspond to the crystallographic orientation (in IPF map) and CI value (in CI map). In the used material file of WC, the crystal structure is hexagonal with a = 0.2906 nm and c = 0.2838 nm. This material file is provided by the collection software for the EBSD pattern (TSL OIM Data Collection Ver 5.31).

hardness values changed after the LD treatment in both easy-to-cut and difficult-to-cut WC-Co surface samples. The catalog value of the Vickers hardness of WC-Co is 1700 HV. The hardness values of the easy-to-cut and difficult-to-cut surface samples were 1800 ± 48 and 1857 ± 45 HV, respectively, indicating that the hardness values increased upon finishing using the CMP grinding wheel. In addition, the hardness of the difficult-to-cut surface samples was higher than that of the easy-to-cut ones. The LD-treated surfaces showed hardness values of 2010 ± 78 and 1977 ± 92 HV for the easy-to-cut and difficult-to-cut surface samples, respectively; these values were higher than those before LD. Thus, hardness for 11.7% easy-to-cut and 6.5% difficult-to-cut samples was enhanced by conducting LD on the WC-Co surface. Recently, Zhang et al. reported that the hardness increased when WC-Co (Co content: 8 wt%) and cBN (20 vol %) were mixed [45]. Meanwhile, the hardness decreased with increasing cBN content above 30 vol% [45]. The addition of an appropriate amount of BN is thought to increase the hardness.

The surface of the WC-Co tool tip was sharpened via CMP processing, resulting in the extension of tool life relative to that before CMP processing [6,7]. Specifically, the cutting speed of Inconel 718 improved by 148% and reduced flank wear by 50% [7]. Moreover, the cutting speed of Ti–6V–4V improved by 150% and reduced flank wear by 43% [7]. Because the hardness of the WC-Co surface increases upon CMP, the increased tool life is attributed to this improvement. In addition, the hardness of the WC-Co surface increased upon LD treatment. In glass processing, a cutting length of 2000 mm was obtained for LD-treated WC-Co, which is considerably higher than (20 mm) for non-LD-treated WC-Co [34]. Even in glass processing, cutting with LD-treated WC-Co extended the tool life by 100 times relative to that before LD [34]. Therefore, the tool life can be improved by increasing the hardness.

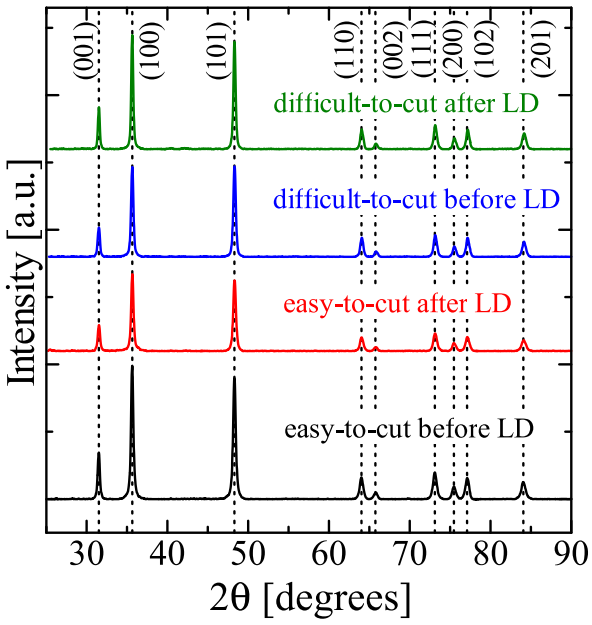

Fig. 4. XRD patterns of the samples before and after LD treatment. The XRD pattern indexed with WC phase (JCPDS file 00-051-0939).

Table 3
Vickers hardness test results of the easy-to-cut and difficult-to-cut samples.

Measuring point	Easy-to-cut [*HV*]		Difficult-to-cut [*HV*]	
	Before LD	After LD	Before LD	After LD
1	1822	2056	1911	2018
2	1801	1993	1854	2109
3	1719	1994	1855	1865
4	1812	2108	1877	1934
5	1844	1899	1788	1957

3.2. Structural changes in laser-irradiated WC-Co surface without BN doping

3.2.1. WC-Co surface structure change by SEM and EBSD

The microstructural change in the WC-Co surface caused by laser irradiation alone was studied through SEM. The micrographs are shown in Fig. 5 (a-1) and (b-1). The number of laser shots was varied using an optical system similar to that shown in Fig. 1 but without conducting BN doping. The WC-Co surface was highly uneven after the laser irradiation treatment alone. Moreover, the WC-Co surface became more uneven as the number of laser shots increased.

Fig. 5 (a-2), (a-3), (b-2), and (b-3) show the EBSD results for the laser-irradiated WC-Co surface. The laser-irradiated WC-Co surface structure did not exhibit any EBSD patterns from the WC structure. A Co_6W_6C (bcc) structure is also observed, which is known as an embrittlement η phase [46]. The EBSD patterns of the WC-Co surface subjected to laser irradiation alone also did not show WC structures. Moreover, the surface structure was altered as the number of laser shots increased.

3.2.2. XRD of laser-irradiated WC-Co surface

The crystal structure at a depth of 0.17 mm from the laser-irradiated WC-Co surface was studied through XRD. The peaks corresponding to WC were observed among other identifiable peaks. Fig. 6 (a), (b), and (c) show the magnified views of these peaks, which were also compared based on the PDF-4 database. Furthermore, the peaks were identified using the CrystalDiffract software and the values of α-WC_{1-x} (a = 0.4266 nm) [47] and β-WC (a = 0.4252 nm) [47]. As shown in Fig. 6, after laser irradiation with 500,000 shots, the α-WC_{1-x} (111), (200), (220); Co_3W_3C (422); and Co_6W_6C (422) peaks were observed. Following laser irradiation with 1,000,000 shots, the β-WC (111), (200), (220), and Co_3W_3C (422) peaks were observed. After 500,000 shots, the Vickers hardness was 1572 ± 58 HV, which is lower than that before laser irradiation, as shown in Table 3. Co_3W_3C and Co_6W_6C have the η phase (embrittlement phase) [46], which possibly decreased the hardness of the sample. Upon laser irradiation, the η phase reportedly transforms to the powder state (WC, Co) [46]. The reaction in the η phase is an inclusion reaction of liquid + θ (W_3Ni_3C) + W = η at approximately 1600 °C (Co melting point 1495 °C) [48], and laser irradiation increased the surface temperature above 1600 °C. From the structural change in the ternary phase diagram [48], we estimated the temperature to be above 1600 °C. Furthermore, γ-WC (α-WC_{1-x} and β-WC) is a structure

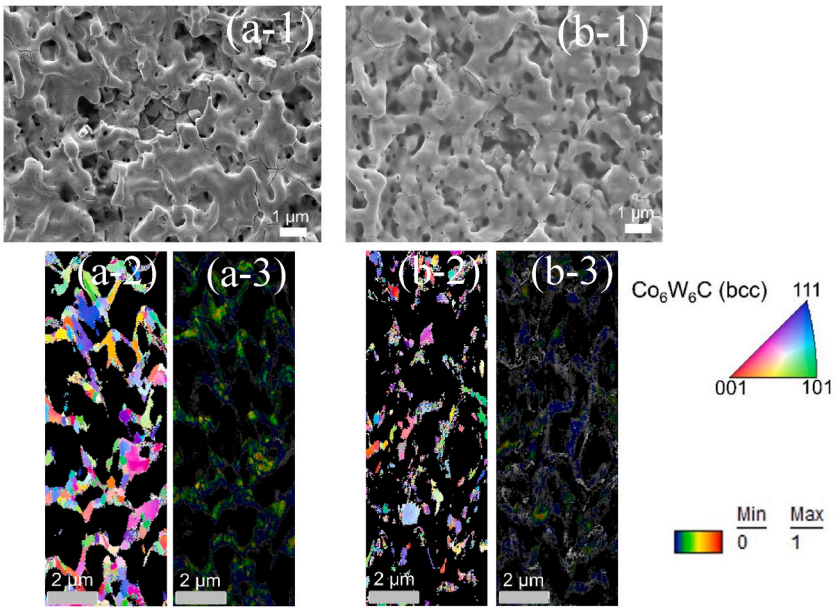

Fig. 5. SEM images after laser irradiation with (a-1) 500,000 and (b-1) 1,000,000 shots. EBSD results after laser irradiation with (a-2, a-3) 500,000 and (b-2, b-3) 1,000,000 shots. (a-2) and (b-2) are the IPF maps, and (a-3) and (b-3) are the CI maps. The colors correspond to crystallographic orientation (in IPF maps) and CI value (in CI maps). In the used material file of Co_6W_6C, the crystal structure is cubic with a = 1.0897 nm. This material file is provided by the collection software for the EBSD pattern (TSL OIM Data Collection Ver 5.31).

[47] that results from the melting of the spark-treated WC-Co surface. The γ-WC structure is also produced on the WC-Co surface by high-intensity pulsed ion beams [30]. Because these treatments are at non-equilibrium, laser irradiation increased the temperature of the WC-Co surface and produced the γ-WC structure. Therefore, the surface structure of the LD-treated WC-Co differs from that of the samples treated with laser irradiation alone and BN could be laser doped on the WC-Co surface.

3.3. WC-Co surface structural changes by LD-treated with 47.5% BN

3.3.1. SEM and EBSD of LD-treated WC-Co

SEM was conducted to observe the LD-treated WC-Co surface with different surface coverages of the doped materials, and EBSD was performed to analyze the surface structure. The SEM of the laser-irradiated WC-Co surface with 47.5% BN is shown in Fig. 7. As shown in Figs. 7 (a-1), after LD treatment with 500,000 shots, the edge of the WC microcrystal structure was convex. Meanwhile, the WC-Co surface after LD treatment with 1,000,000 shots became more uneven, as shown in Figs. 7 (b-1). Thus, increasing the number of laser shots led to an uneven surface.

Fig. 7 (a-2) to (a-5) and (b-2) to (b-5) show the EBSD profiles of the laser-irradiated WC-Co surfaces subjected to 47.5% BN doping. Fig. 7 (a-3) shows that the map of the LD-treated WC-Co surface after 500,000 shots has several areas with low CI values owing to WC and some areas with high CI values. The IPF map of the WC structure is shown in Figs. 7 (a-2). Moreover, areas with the CI values arising from Co_6W_6C are only partially observed in the CI maps shown in Figs. 7 (a-5). As shown in Figs. 7 (b-3), the CI value owing to WC was low, and minimal WC structure could be observed in the map. Meanwhile, Figs. 7 (b-5) shows that the LD-treated WC-Co surface after 1,000,000 shots has low CI values for Co_6W_6C in some areas and high CI values elsewhere. The Co_6W_6C structure was observed in the IPF maps shown in Figs. 7 (b-4). As the surface coverage of BN increased, structures other than WC were observed. Furthermore, the surface structure changed more as the number of laser shots increased.

3.3.2. XRD of LD-treated WC-Co surface

The crystal structure of the LD-treated WC-Co with 47.5% BN was studied through XRD. Based on the X-ray absorption rate, the structure is observed at a depth of 0.17 mm from the surface. We observed peaks for the WC structure of the LD-treated workpieces with different surface coverage areas of doping materials. As described in Section 3.2.2, peaks other than those of the WC structure were also observed, as shown in an enlarged version of Fig. 8(a), (b), and (c). Following the LD treatment with 500,000 shots, the α-WC_{1-x}: (111), (200), (220) and Co_3W_3C (422) peaks were observed. After the LD treatment with 1,000,000 shots, the α-WC_{1-x}: (111), (200), (220); β-WC: (111), (200), (220); and Co_3W_3C (422), B_8C (271), B_4C (303) peaks were observed. Because the position of the unidentified peak after LD is the same as that of the peak after laser irradiation alone with 1,000,000 shots, the structure is derived from WC-Co. The Vickers hardness values after the LD treatment with 500,000 and 1,000,000 shots were 1584 ± 35 and 1567 ± 17 HV, respectively. This indicates that the hardness of the samples after doping with 47.5% BN is lower than that before and after LD with 34.8% BN. Furthermore, Co_3W_3C in the η phase (embrittlement phase) [46] accounts for the low hardness. Following LD, the η-phase

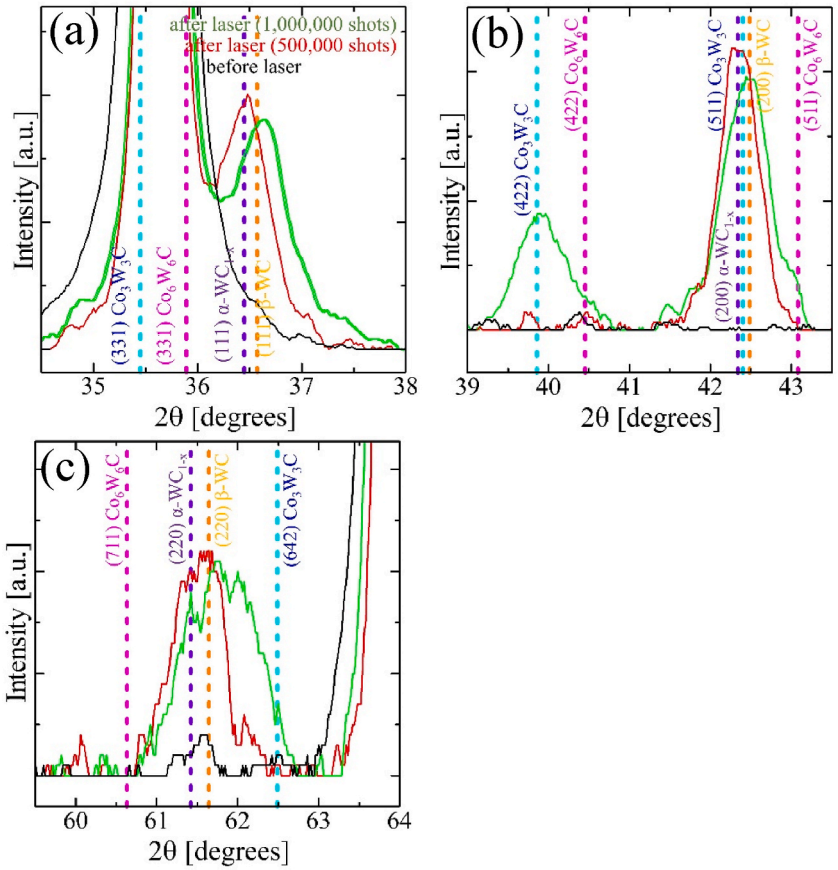

Fig. 6. XRD patterns before and after laser irradiation at different 2θ ranges: (a) 34.5°–38.0°; (b) 39.0°–43.5°; and (c) 59.5°–64.0°. Black, red, and green curves respectively correspond to the XRD peaks before and after irradiation with 500,000 and 1,000,000 shots. The XRD pattern indexed with WC (JCPDS file 00-051-0939), Co_6W_6C (JCPDS file 00-022-0597), and Co_3W_3C (JCPDS file 00-027-1125) phases.

and γ-WC structures were formed in addition to the WC structure at 47.5% BN, and differences in the surface structure were observed compared with 34.8% BN. Moreover, the surface structure differs from that upon laser irradiation alone. EBSD measurements for 1,000,000 laser shots and at 34.8% BN could not be performed because the uneven surface hinders the observation of EBSD patterns. Meanwhile, only peaks derived from the WC structure were observed in the XRD patterns. These differences are better understood in terms of the thermal conductivity and specific heat. The thermal conductivity of WC-Co is 79 W/m·K (catalog value) and the specific heat values [49] are 192 J/kg·K (Co 5%, 347.5 K) and 189 J/kg·K (Co 7%, 398 K). The thermal conductivity of BN is 14 W/m·K [50] and 20 W/m·K [51], and the specific heat is 791 J/kg·K (300 K) [52]. The thermal conductivity of BN also varies with film thickness [53]. Because BN has high specific heat and low thermal conductivity, the high BN concentration and high coverage of WC-Co cause heat to accumulate on the surface, which changes the surface structure owing to the annealing effect caused by the increasing temperature.

The penetration length of the laser (λ = 532 nm) to W is 15.77 nm (λ = 539.1 nm, k = 2.72 [54]). Meanwhile, the penetration lengths to BN are 0.08 μm (λ = 500.0 nm, k = 0.05 [55]) and 1.04 μm (λ = 550.0 nm, k = 0.042 [55]). Because BN is only applied to the surface of WC-Co, the adhesion is weak. The pulse duration of the laser is 500 ps, and BN begins to be ablated from the surface of the coating layer after the pulses begin to be delivered. Because the particle size of BN is approximately 0.1 μm, the laser penetrates the BN layer when the BN film becomes thin during ablation and excites both the BN particles adsorbed on the metal (WC, Co) surface and the metal layer. As a result, BN is doped into the metal surface layer. Moreover, as the laser continues to illuminate the metal surface, the temperature of the substrate surface reaches the required temperature to diffuse BN, resulting in BN diffusion beyond the transmission length. The LD treatment is performed in a non-thermal equilibrium state with short-time photoexcitation on the order of 500 ps, which cannot be fitted by the diffusion equation of the thermal equilibrium state [33,56]. The higher the number of shots, the more likely it is that the surface structure will change due to laser irradiation [57].

4. Conclusions

By applying semiconductor technology as a finishing method for WC-Co tool edges, flatness was achieved while maintaining the

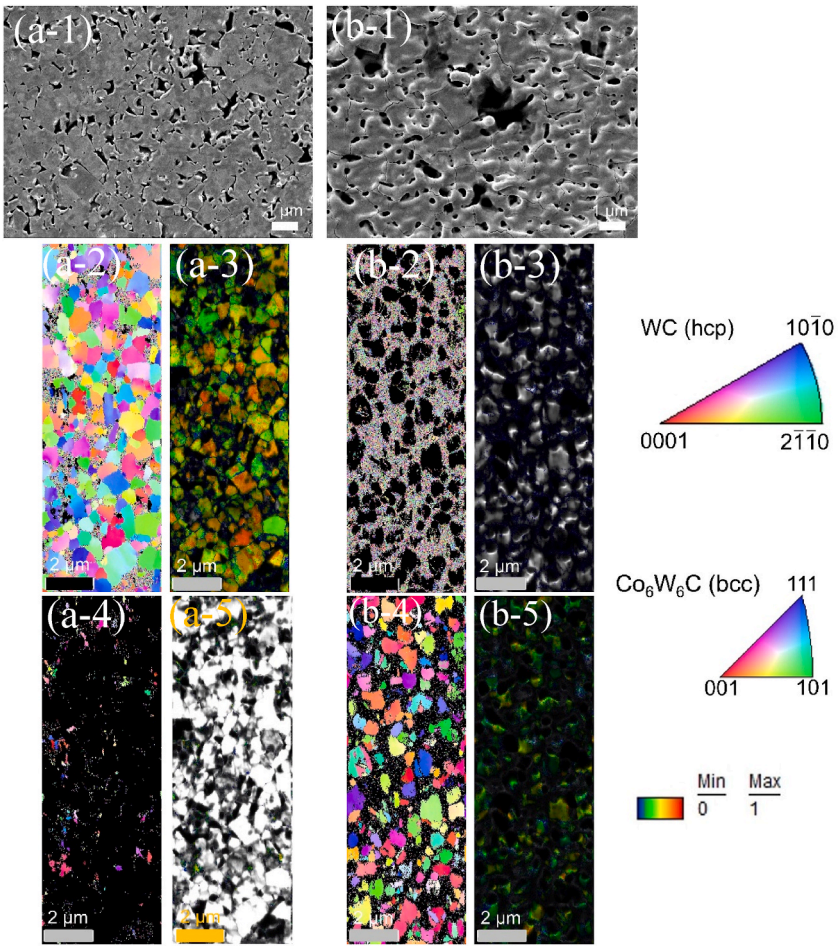

Fig. 7. SEM images after the LD treatment with 47.5% BN and after laser irradiation with (a-1) 500,000 shots and (b-1) 1,000,000 shots. EBSD patterns after the LD with 47.5% BN and after laser irradiation with (a-2 to a-5) 500,000 and (b-2 to b-5) 1,000,000 shots: (a-2), (a-3), (b-2), and (b-3) are the maps of the WC structure, while (a-4), (a-5), (b-4), and (b-5) are the maps of the Co_6W_6C structure. Moreover, (a-2), (a-4), (b-2), and (b-4) are the IPF maps, while (a-3), (a-5), (b-3), and (b-5) are the CI maps. The colors correspond to the crystallographic orientation (in IPF maps) and CI value (in CI maps). In the used material file of WC, the crystal structure is hexagonal with a = 0.2906 nm and c = 0.2838 nm. In the case of Co_6W_6C, the crystal structure is cubic with a = 1.0897 nm. These materials files are provided by the collection software for the EBSD pattern (TSL OIM Data Collection Ver 5.31).

WC structure without introducing machining strain to the topmost surface. The XRD and EBSD measurements did not reveal any difference in surface structure between the easy-to-cut and hard-to-cut samples. The hardness of the WC-Co surface finished by the CMP wheel was improved by 5.88% for the easy-to-cut and 9.24% for the difficult-to-cut samples. The crystal structure of WC-Co was changed by LD with 34.5% BN, and the hardness was improved by 11.7% for the easy-to-cut samples and 6.5% for the difficult-to-cut samples. The η phase was observed among other structures on the WC-Co surface treated by laser irradiation without BN doping. The same η phase was observed for the LD with 47.5% BN concentration. The Vickers hardness decreased by 12.67% for laser irradiation alone and by 14.70% for LD with 47.5% BN compared with that before processing (after CMP processing). Surface modification via LD preserves the WC structure up to a depth of 50 nm and is suitable for cutting tool materials. Thus, doping can be performed on the tool tip while maintaining the structure of WC. The results show that maintaining the WC structure improves the performance of the tool material. The EDS analysis and XRD results could not clarify whether BN diffused in the WC or Co phase. We would like to clarify the depth direction and BN diffusion after LD treatment in future research projects.

Author contribution statement

Yayoi Tanaka: Performed the experiments; Analyzed and interpreted the data; Wrote the paper.

Hisashi Sato: Performed the experiments; Analyzed and interpreted the data; Contributed reagents, materials, analysis tools or data.

Osamu Eryu: Conceived and designed the experiments; Analyzed and interpreted the data; Contributed reagents, materials,

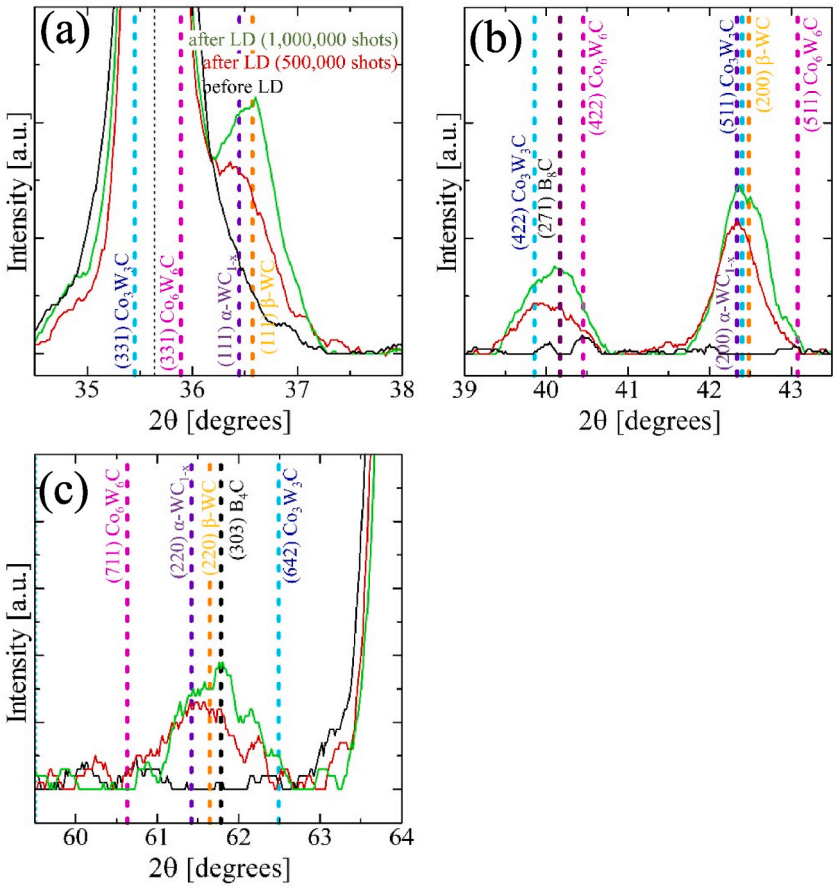

Fig. 8. XRD patterns before and after LD with 47.5% BN at different 2θ ranges: (a) 34.5°–38.0°; (b) 39.0°–43.5°; and (c) 59.5°–64.0°. Black, red, and green curves respectively correspond to the XRD peaks before irradiation and after irradiation with 500,000 and 1,000,000 shots. The XRD pattern indexed with WC (JCPDS file 00-051-0939), Co_6W_6C (JCPDS file 00-022-0597), Co_3W_3C (JCPDS file 00-027-1125), B_4C (JCPDS file 00-035-0798) and B_8C (JCPDS file 00-026-0232) phases.

analysis tools or data.

Data availability statement

No data was used for the research described in the article.

Funding

This work was partly supported by the Ministry of Economy, Trade, and Industry (METI) Monozukuri R&D Support Grant Program for SMEs.

Declaration of competing interest

The authors declare that they have no known competing financial interests or personal relationships that could have appeared to influence the work reported in this paper.

Acknowledgements

This work was partially supported by the Ministry of Economy, Trade, and Industry's (METI) Monozukuri R&D Support Grant Program for SMEs. The authors acknowledge the cooperation of C.K.K Co. Ltd. and Mr. Shuji Sawada for the construction of the laser system. The authors would like to acknowledge the cooperation of the Organization for Co-Creation Research and Social Contributions, Nagoya Institute of Technology, and Dr. Yoko Sakurai for the EDS analysis and Monte Carlo simulations of the sample for the depth approximation.

References

[1] H. Nie, T. Zhang, Development of manufacturing technology on WC–Co hardmetals, Tungsten 1 (2019) 198–212, https://doi.org/10.1007/s42864-019-00025-6.

[2] T. Klünsner, T. Lube, C. Gettinger, L. Walch, R. Pippan, Influence of WC-Co hard metal microstructure on defect density, initiation and propagation kinetics of fatigue cracks starting at intrinsic and artificial defects under a negative stress ratio, Acta Mater. 188 (2020) 30–39, https://doi.org/10.1016/j.actamat.2020.01.057.

[3] T. Kagnaya, C. Boher, L. Lambert, M. Lazard, T. Cutard, Wear mechanisms of WC–Co cutting tools from high-speed tribological tests, Wear 267 (2009) 890–897, https://doi.org/10.1016/j.wear.2008.12.035.

[4] J.B.J.W. Hegeman, J.T.M. De Hosson, G. de With, Grinding of WC–Co hardmetals, Wear 248 (2001) 187–196, https://doi.org/10.1016/S0043-1648(00)00561-5.

[5] J. Yang, M. Odén, M.P. Johansson-Jõesaar, L. Llanes, Grinding effects on surface integrity and mechanical strength of WC-Co cemented carbides, Procedia C.I.R.P. 13 (2014) 257–263, https://doi.org/10.1016/j.procir.2014.04.044.

[6] O. Eryu, Nanofabrication technology for aircraft parts, Bull. JSTP 3 (2020) 75–78, https://doi.org/10.32277/plastos.3.26_75 [Japanese].

[7] Y. Tanaka, H. Sato, O. Eryu, Improved cemented carbide tool edge formed by solid phase chemical–mechanical polishing, J. Mater. Res. Technol. 20 (2022) 606–615, https://doi.org/10.1016/j.jmrt.2022.07.077.

[8] M.J. Bermingham, S. Palanisamy, M.S. Dargusch, Understanding the tool wear mechanism during thermally assisted machining Ti-6Al-4V, Int. J. Mach. Tool Manufact. 62 (2012) 76–87, https://doi.org/10.1016/j.ijmachtools.2012.07.001.

[9] D. Jianxin, L. Yousheng, S. Wenlong, Diffusion wear in dry cutting of Ti-6Al-4V with WC/Co carbide tools, Wear 265 (2008) 1776–1783, https://doi.org/10.1016/j.wear.2008.04.024.

[10] A. Li, J. Zhao, H. Luo, Z. Pei, Z. Wang, Progressive tool failure in high-speed dry milling of Ti-6Al-4V alloy with coated carbide tools, Int. J. Adv. Manuf. Technol. 58 (2012) 465–478, https://doi.org/10.1007/s00170-011-3408-1.

[11] P. Olander, J. Heinrichs, On wear of WC–Co cutting inserts in turning of Ti6Al4V–a study of wear surfaces, Tribol. Mater. Surface Interfac. 15 (2021) 181–192, https://doi.org/10.1080/17515831.2020.1830251.

[12] S. Zhang, J.F. Li, J. Sun, F. Jiang, Tool wear and cutting forces variation in high-speed end-milling Ti-6Al-4V alloy, Int. J. Adv. Manuf. Technol. 46 (2010) 69–78, https://doi.org/10.1007/s00170-009-2077-9.

[13] K. Hotta, K. Hirose, Y. Tanaka, K. Kawata, O. Eryu, Improvements in electrical properties of SiC surface using mechano-chemical polishing, Mater. Sci. Forum 600 (603) (2008) 823–826. https://doi.org/10.4028/www.scientific.net/MSF.600-603.823.

[14] Y. Tanaka, T. Kanda, K. Nagatoshi, M. Yoshimura, O. Eryu, The atomic step induced by off angle CMP influences the electrical properties of the SiC surface, Mater. Sci. Forum 717–720 (2012) 569–572. https://doi.org/10.4028/www.scientific.net/MSF.717-720.569.

[15] J. Sun, J. Zhao, Z. Huang, K. Yan, X. Shen, J. Xing, Y. Gao, Y. Jian, H. Yang, B. Li, A review on binderless tungsten carbide: development and application, Nano-Micro Lett. 12 (2020) 13, https://doi.org/10.1007/s40820-019-0346-1.

[16] V. Bushlya, J. Zhou, J.E. Ståhl, Effect of cutting conditions on machinability of superalloy Inconel 718 during high speed turning with coated and uncoated PCBN tools, Procedia C.I.R.P. 3 (2012) 370–375, https://doi.org/10.1016/j.procir.2012.07.064.

[17] C.H.C. Che Haron, A. Ginting, J.H. Goh, Wear of coated and uncoated carbides in turning tool steel, J. Mater. Process. Technol. 116 (2001) 49–54, https://doi.org/10.1016/S0924-0136(01)00841-X.

[18] S. do Nascimento Rosa, A.E. Diniz, D. Neves, B.B. Salles, S.S. Guerreiro, Analysis of the life of cemented carbide drills with modified surfaces, Int. J. Adv. Manuf. Technol. 71 (2014) 2125–2136, https://doi.org/10.1007/s00170-013-5598-1.

[19] K.-D. Bouzakis, G. Skordaris, N. Michailidis, A. Asimakopoulos, G. Erkens, Effect on PVD coated cemented carbide inserts cutting performance of micro-blasting and lapping of their substrates, Surf. Coat. Technol. 200 (2005) 128–132, https://doi.org/10.1016/j.surfcoat.2005.02.119.

[20] H.K. Tönshoff, A. Mohlfeld, Surface treatment of cutting tool substrates, Int. J. Mach. Tool Manufact. 38 (1998) 469–476, https://doi.org/10.1016/S0890-6955(97)00091-6.

[21] S.K. Mishra, S. Ghosh, S. Aravindan, Physical characterization and wear behavior of laser processed and PVD coated WC/Co in dry sliding and dry turning processes (2019) 93–110, https://doi.org/10.1016/j.wear.2019.03.008. Wear 428–429.

[22] B. Breidenstein, C. Gey, B. Denkena, Residual stress development in laser machined PVD-coated carbide cutting tools, Mater. Sci. Forum 768–769 (2013) 391–397. https://doi.org/10.4028/www.scientific.net/MSF.768-769.391.

[23] Q. Wan, M. Zheng, S. Yang, Thermal effect analysis of laser processing cemented carbide micro-texture, Int. J. Heat Technol. 37 (2019) 71–76, https://doi.org/10.18280/ijht.370108.

[24] K. Zhang, J. Deng, J. Sun, C. Jiang, Y. Liu, S. Chen, Effect of micro/nano-scale textures on anti-adhesive wear properties of WC/Co-based TiAlN coated tools in AISI 316 austenitic stainless steel cutting, Appl. Surf. Sci. 355 (2015) 602–614, https://doi.org/10.1016/j.apsusc.2015.07.132.

[25] E. Cappelli, S. Orlando, F. Pinzari, A. Napoli, S. Kaciulis, WC–Co cutting tool surface modifications induced by pulsed laser treatment, Appl. Surf. Sci. 138–139 (1999) 376–382, https://doi.org/10.1016/S0169-4332(98)00607-2.

[26] M. Nizar, N. Arimatsu, H. Kawamitsu, K. Takai, M. Fukumoto, Study on optimal surface property of WC-Co cutting tool for aluminum alloy cutting, IOP Conf. Ser. Mater. Sci. Eng. 114 (2016), 12024, https://doi.org/10.1088/1757-899X/114/1/012024.

[27] P. Butler-Smith, D. Khaemba, T.L. See, N.Z. Yussefian, R. Gaddam, J.G. Vilar, The influence of femtosecond laser produced periodic surface textures on cutting tool friction, Procedia C.I.R.P. 95 (2020) 885–890, https://doi.org/10.1016/j.procir.2020.01.187.

[28] D. Ye, Y. Lijun, C. Bai, W. Xiaoli, W. Yang, X. Hui, Investigations on femtosecond laser-modified microgroove-textured cemented carbide YT15 turning tool with promotion in cutting performance, Int. J. Adv. Manuf. Technol. 96 (2018) 4367–4379, https://doi.org/10.1007/s00170-018-1906-0.

[29] C. Deng, P. Molian, Laser shock wave treatment of polycrystalline diamond tool and nanodiamond powder compact, Int. J. Adv. Manuf. Technol. 63 (2012) 259–267, https://doi.org/10.1007/s00170-012-3904-y.

[30] A.I. Prima, YuI. Egorova, A.I. Pushkarev, S.V. Matryenin, Modification of the WC-Co carbide surface with high-intensity pulsed ion beam, J. Phys.: Conf. Ser. 1588 (2020), 12045, https://doi.org/10.1088/1742-6596/1588/1/012045.

[31] H. Hagino, T. Yamaguchi, Studies of laser surface modification, J. Vac. Soc. Jpn. 56 (2013) 315–321, https://doi.org/10.3131/jvsj2.56.315 [Japanese].

[32] M. Law, R. Karthik, S. Sharma, J. Ramkumar, Finish turning of hardened bearing steel using textured PcBN tools, J. Manuf. Process. 60 (2020) 144–161, https://doi.org/10.1016/j.jmapro.2020.10.051.

[33] O. Eryu, Y. Okuyama, K. Nakashima, T. Nakata, M. Watanabe, Formation of a *p-n* junction in silicon carbide by aluminum doping at room temperature using a pulsed laser doping method, Appl. Phys. Lett. 67 (1995) 2052–2053, https://doi.org/10.1063/1.115075.

[34] Y. Tanaka, H. Sato, O. Eryu, Effect of LD Processing on Cutting of Cemented Carbide Tools, the 23rd International Symposium on Advances in Abrasive Technology, Nov. 30–Dec. 3, Niseko, Hokkaido, Japan, 2021, pp. 418–422.

[35] C. Gorecki, S. Bargiel, MEMS scanning mirrors for optical coherence tomography, Photonics 8 (2021) 6, https://doi.org/10.3390/photonics8010006.

[36] M. Gasgnier, H. Szwarc, A. Ronez, Low-energy ball-milling: transformations of boron nitride powders, Crystallographic and chemical, J. Mater. Sci. 35 (2000) 3003–3009, https://doi.org/10.1023/A:1004735011914.

[37] J. Ghosh, S. Mazumdar, M. Das, S. Ghatak, A.K. Basu, Microstructural characterization of amorphous and nanocrystalline boron nitride prepared by high energy ball milling, Mater. Res. Bull. 43 (2008) 1023–1031, https://doi.org/10.1016/j.materresbull.2007.04.022.

[38] J. Qin, X. Wang, Q. Jiang, M. Cao, Optimizing dispersion, exfoliation, synthesis, and device fabrication of inorganic nanomaterials using hansen solubility parameters, ChemPhysChem 20 (2019) 1069–1097, https://doi.org/10.1002/cphc.201900110.

[39] J.M. Johnston, S.A. Catledge, Metal-boride phase formation on tungsten carbide (WC-Co) during microwave plasma chemical vapor deposition, Appl. Surf. Sci. 364 (2016) 315–321, https://doi.org/10.1016/j.apsusc.2015.12.156.

[40] K. Rychlik, C. Senderowski, Wear Analysis of gun barrel drill blade in 1.0503 steel drilling process in Milpro HG12 oil environment with addition of ultra-dispersive copper particles and copper oxides, Tech. Sci. 22 (2019) 221–235, https://doi.org/10.31648/ts.4966.
[41] G. Cassabois, P. Valvin, B. Gil, Hexagonal boron nitride is an indirect bandgap semiconductor, Nat. Photonics 10 (2016) 262–266, https://doi.org/10.1038/nphoton.2015.277.
[42] T. Ida, How to use powder diffraction method (2)–preparation of specimen, J. Flux Growth 3 (2008) 50–55 [Japanese].
[43] D.C. Creagh, J.H. Hubbell, X-ray absorption (or attenuation) coefficients, in: E. Prince (Ed.), International Tables for Crystallography Volume C: Mathematical, Physical, and Chemical Tables, International Union of Crystallography, 2006, pp. 220–229.
[44] Z.M. Zhang, X.C. He, H.S. Shen, F.H. Sun, M. Chen, Y.Z. Wan, Pre-treatment for diamond coatings on free-shape WC-Co tools, Diam. Relat. Mater. 9 (2000) 1749–1752, https://doi.org/10.1016/S0925-9635(00)00328-9.
[45] J.F. Zhang, R. Tu, T. Goto, Spark plasma sintering and characterization of WC-Co-cBN composites, Key Eng. Mater. 616 (2014) 194–198. https://doi.org/10.4028/www.scientific.net/KEM.616.194.
[46] Y. Yang, C. Zhang, D. Wang, L. Nie, D. Wellmann, Y. Tian, Additive manufacturing of WC-Co hardmetals: a review, Int. J. Adv. Manuf. Technol. 108 (2020) 1653–1673, https://doi.org/10.1007/s00170-020-05389-5.
[47] A.S. Kurlov, A.I. Gusev, Tungsten carbides and W-C phase diagram, Inorg. Mater. 42 (2006) 121–127, https://doi.org/10.1134/S0020168506020051.
[48] P. Rautala, J.T. Norton, Tungsten-cobalt-carbon system, JOM 4 (1952) 1045–1050, https://doi.org/10.1007/BF03397766.
[49] Y.S. Touloukian, E.H. Buyco, Thermophysical properties of matter – the TPRC data series, Specific Heat-Nonmetallic Solids 5 (1970) 1282–1284. IFI, New York. Plenum.
[50] Y. Wang, L. Xu, Z. Yang, H. Xie, P. Jiang, J. Dai, W. Luo, Y. Yao, E. Hitz, R. Yang, B. Yang, L. Hu, High temperature thermal management with boron nitride nanosheets, Nanoscale 10 (2018) 167–173, https://doi.org/10.1039/c7nr07058f.
[51] J.-C. Zheng, L. Zhang, A.V. Kretinin, S.V. Morozov, Y.B. Wang, T. Wang, X. Li, F. Ren, J. Zhang, C.-Y. Lu, J.-C. Chen, M. Lu, H.-Q. Wang, A.K. Geim, K. S. Novoselov, High thermal conductivity of hexagonal boron nitride laminates, 2D Mater. 3 (2016), 11004, https://doi.org/10.1088/2053-1583/3/1/011004.
[52] R.A. McDonald, D.R. Stull, The heat content and heat capacity of boron nitride from 298 to 1689°K.[1], J. Phys. Chem. 65 (1961) 1918, https://doi.org/10.1021/j100827a518.
[53] H. Dong, P. Hirvonen, Z. Fan, T. Ala-Nissila, Heat transport in pristine and polycrystalline single-layer hexagonal boron nitride, Phys. Chem. Chem. Phys. 20 (2018) 24602–24612, https://doi.org/10.1039/c8cp05159c.
[54] E.D. Palik (Ed.), Handbook of Optical Constants of Solids, Academic Press, INC., 1985, p. 366.
[55] J.J. Pouch, S.A. Alterovitz, K. Miyoshi, J.O. Warner, Boron nitride: composition, optical properties, and mechanical behavior, MRS Online Proc. Libr. (1987) 323–328, https://doi.org/10.1557/PROC-93-323.
[56] M. Uehlein, S.T. Weber, B. Rethfeld, Influence of electronic non-equilibrium on energy distribution and dissipation in aluminum studied with an extended two-temperature, Model 12 (2022) 1655, https://doi.org/10.3390/nano12101655.
[57] F. Wang, C. Zhang, Y. Lu, M. Nastasi, B. Cui, Laser shock processing of polycrystalline alumina ceramics, J. Am. Ceram. Soc. 100 (2017) 911–919, https://doi.org/10.1111/jace.14630.